

Dynamic Soaring of Sailplanes over Open Fields

Pritam P. Sukumar* and Michael S. Selig[†]

University of Illinois at Urbana-Champaign, Urbana, IL 61801, USA

Dynamic soaring of a sailplane in the earth's atmospheric boundary layer was computationally investigated over a range of conditions to explore the feasibility of flying over a large vertical extent over open fields. A point-mass sailplane model was studied as well as a full six degree-of-freedom (6-DOF) piloted sailplane model. For the point-mass model, parameter sweeps were performed around a baseline 3-m (9.58-ft) wingspan sailplane having a weight of 15 kg (33 lb) and aspect ratio of 20. Results from the point-mass model show that in certain high wind conditions, dynamic soaring energy-conserving orbits are possible for flight trajectories extending from the ground to 185 m (607 ft) aloft. A 6-DOF piloted flight simulator was used, and it produced similar results that showed dynamic soaring over open fields for large vertical extents. Together these results support the conclusion that it is possible to perform dynamic soaring in high wind conditions through the full extent of the atmospheric boundary layer to high altitudes over open land with model-scale unpowered sailplanes having both high wing loadings and high lift-to-drag ratios.

Nomenclature

AR	=	aspect ratio
a	=	wind shear parameter
b	=	wingspan
C_{D_0}	=	parasite drag coefficient
D	=	drag
e	=	wing planform efficiency factor
g	=	gravitational acceleration
h_e	=	energy height ($= V^2/2g + z$)
L	=	lift
L/D	=	lift-to-drag ratio
m	=	mass
n	=	normal load factor ($= L/W$)
r	=	aircraft-relative radius of dynamic soaring orbit ground trace
S	=	wing area
U	=	wind speed
$U(z)$	=	wind profile
U_{ref}	=	reference wind speed
V	=	airspeed, relative wind
W	=	weight
x, y, z	=	position coordinates
z_0	=	roughness factor for boundary layer
z_{ref}	=	reference height

*Graduate Student, Department of Aerospace Engineering, 104 S. Wright St. Member AIAA.

[†]Associate Professor, Department of Aerospace Engineering, 104 S. Wright St. Senior Member AIAA.
<http://www.ae.illinois.edu/m-selig>

Subscripts

D = value at dwell

Symbols

ϕ, γ, ψ = bank angle, flight path angle, heading angle

γ_1, γ_2 = dynamic soaring rule parameters

v = ratio of wind speed to reference wind speed

ζ = ratio of height to reference height

Superscripts

$(\cdot)'$ = gradient with respect to height

$(\dot{\cdot})$ = time derivative

I. Introduction

Soaring can be defined as flight in which an internal thrust mechanism is not present. The aircraft thus needs to be capable of extracting energy from the atmosphere if it has to stay aloft. The earliest observations of soaring were made by Lord Rayleigh based on the flight patterns of birds.¹ He hypothesized that the wind must be non-uniform in order to gain energy from the atmosphere. The flight of albatrosses in particular seemed to point toward a consistent mechanism for extracting energy from vertical wind gradients. The maneuvers involved in albatross flight were studied, and dynamic soaring as a mechanism for extraction of energy from wind shear was investigated. Hendriks^{2,3} showed that dynamic soaring orbits that are periodic with respect to energy are possible.

Finding the minimum wind shear required to perform dynamic soaring posed a challenging numerical problem because of the coupled and nonlinear nature of the equations of motion. Optimal control was used to demonstrate that the shear commonly present over open seas was sufficient to allow an albatross to perform dynamic soaring.⁴ Barnes⁵ formulated classes of trajectories that simulated orbits flown by albatrosses in their daily flights. Lissaman⁶ considered the cases of a step increase and continuous variation of wind speed in the boundary layer. He derived expressions for the minimum wind shear required for dynamic soaring in these conditions. More recently, Denny⁷ studied dynamic soaring from a simplified point of view assuming a constant lift-to-drag ratio and dividing the trajectory into segments.

For full-scale aircraft, it was shown by Sachs,⁸ that dynamic soaring by full-size sailplanes is possible with values of wind shear found near mountain ridges. Nonlinear optimal control methods have also been used to model dynamic soaring as an optimization problem with the final time and altitude as cost functions for full-size UAVs.⁹ This approach for a full-sized UAV⁹ was extended by Akhtar, et al.,¹⁰ wherein they developed trajectory tracking algorithms that could be implemented in realtime. Dynamic soaring for powered airplanes with the goal of minimizing the thrust required has been studied using parameter optimization.¹¹ Gordon¹² presented results from full-scale tests and computer simulations of an L-23 Super Blanik sailplane.

Utilization of dynamic soaring by humans has been largely limited to radio controlled (RC) sailplanes because of the high flight speeds required in close proximity to the ground. As reported by Wurts,¹³ he pioneered RC sailplane dynamic soaring in wind shear developed on the leeward side of a windy ridge. Flight speeds near 322 km/hr (200 mph) were reported by him. In an interesting article, Fogel¹⁴ speculates on the possibility of dynamic soaring using RC sailplanes, apparently not aware that it had already been successfully performed. Since this point, dynamic soaring of RC sailplanes has been an ongoing subject of research. Sachs and Mayrhofer^{15,16} discuss optimal trajectories for RC-size sailplanes flying in wind shear like that over a ridge. Wurts collaborated with Boslough¹⁷ who conducted dynamic soaring tests and computer simulations on an 2.4-m (8-ft) span RC sailplane. Parle¹⁸ conducted preliminary flight tests with an RC sailplane and published data showing successful completion of energy conserving oval trajectories. Pilots flying RC sailplanes in dynamic soaring conditions over mountain ridges have continued to push flight speeds to higher limits. In fact, the current highest recorded speed is set at 716 km/hr (445 mph).[‡]

[‡]As reported on the website <http://www.rcspeeds.com/>, the top three speeds set by three different pilots for dynamic soaring with RC sailplanes are 716, 689, 647 km/hr (445, 428, 402 mph). These records were all set this year at Weldon Hill, Lake Isabella, CA with the same sailplane design – Kinetic100 having a 2.54-m span (100 in), aspect ratio of 13.69, and wing loading of 11.9 kg/m² (39 oz/ft²).

As shown in this paper, rather than exploiting the effects of dynamic soaring to dramatically increase flight speed, the energy gain can be used to fly over nearly the entire vertical extent of the atmospheric boundary layer over open fields, that is, from ground elevation to surprisingly high altitudes.¹⁹ Throughout the remainder of this paper, this kind of dynamic soaring will be called ‘high-altitude dynamic soaring.’ A baseline 3-DOF point-mass sailplane model is defined and used in a high-altitude dynamic soaring analysis. Trends are presented and discussed to illustrate the dependence of dynamic soaring performance on both the aircraft and orbit-trajectory parameters. These results are extended to a full 6-DOF realtime flight simulation to validate the possibility of performing high-altitude dynamic soaring over windy open fields like those found all over the Midwestern United States.

II. Point-Mass Dynamic Soaring Model

A. Mathematical Formulation and Trajectory Prescription

The development of the method presented in this section closely follows that presented by Barnes.⁵ The wind is assumed to be directed along the negative x -axis from left to right. The equations of motion used in much of the research on dynamic soaring^{5,7,9,17,20} are most conveniently expressed in the wind-aligned (wind-fixed) axis system²¹ as

$$m\dot{U} \cos \gamma \cos \psi - mg \sin \gamma - D = m\dot{V} \quad (1)$$

$$L \cos \phi - mg \cos \gamma - m\dot{U} \cos \psi \sin \gamma = mV\dot{\gamma} \quad (2)$$

where γ is the flight path angle, ϕ is the bank angle, and ψ is the heading. The term \dot{U} can be expanded as

$$\frac{dU}{dt} = \frac{dU}{dz} \frac{dz}{dt} = U'V \sin \gamma \quad (3)$$

The full term $m\dot{U} \cos \gamma \cos \psi$ on the left hand side in Eq. (1) can be termed the ‘dynamic soaring thrust.’⁵ The name is used in this development because this force term increases the airspeed when the aircraft is gaining energy from dynamic soaring. The second term in Eq. (1) represents the force due to gravity, and the third term is the drag.

While Barnes uses the term dynamic soaring thrust in the wind-aligned axis for the aforementioned quantity $m\dot{U} \cos \gamma \cos \psi$, the physical interpretation of $m\dot{U} \cos \gamma \cos \psi$ is not immediately easy to grasp. However, it is clear in the body-fixed system that the inertial speed and wind speed sum up to produce a relative wind that gives rise to forward tilting of the lift vector in the direction of flight (lift is perpendicular to relative wind). This effect is shown in Fig. 1. The component of this lift in the direction of flight produces in effect ‘thrust,’ that is, dynamic soaring thrust. Whether this force is resolved in the wind-aligned or body-fixed system, it is this force that gives rise to energy extraction from wind shear, in this case, wind shear in a atmospheric boundary layer. As long as there is misalignment between the relative wind and inertial speed as shown in Fig. 1, there will be ‘thrust’ that literally propels the airplane forward. But as the wind begins to overcome the sailplane and cause it to drift downwind, the misalignment goes to zero and the energy extraction stops at that point and energy dissipation returns.

Continuing with the development in Ref. 5, the heading can be related to the velocity and wind-relative radius of curvature by

$$\dot{\psi} = \frac{V \cos \gamma}{r} \quad (4)$$

where r is the airplane-relative turn radius on the ground. The load factor and the bank angle are given by

$$n = \frac{(V/g)\dot{\gamma} + \cos \gamma + (U'V/g) \sin^2 \gamma \cos \psi}{\cos \phi} \quad (5)$$

$$\phi = \arctan \left[\frac{\dot{\psi} + U' \tan \gamma \sin \psi}{(\dot{\gamma}/\cos \gamma) + (g/V) + U' \sin \gamma \tan \gamma \cos \psi} \right] \quad (6)$$

The aircraft position in the ground frame can be found by integrating the velocities along the inertial axes. The velocities in this reference frame can be expressed in terms of the heading ψ , flight path angle γ , airspeed

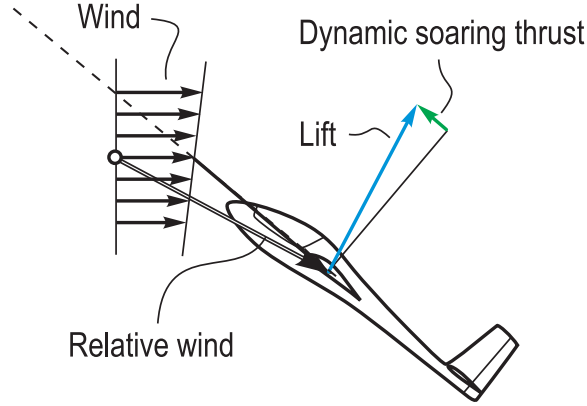


Figure 1. Dynamic soaring thrust (lift vector forward tilt) produced by the misalignment of relative wind and flight path trajectory.

V , and wind speed U as

$$\begin{aligned}\dot{x} &= -V \cos \gamma \cos \psi + U \\ \dot{y} &= V \cos \gamma \sin \psi \\ \dot{z} &= V \sin \gamma\end{aligned}\tag{7}$$

For the aircraft to gain energy from dynamic soaring, the dynamic soaring thrust term from Eq. (1) must be positive for a substantial portion of the orbit. Moreover, in that equation it can be seen that to satisfy this condition, the flight path angle should be positive when the aircraft is facing the wind and negative otherwise. Thus, the aircraft must ascend upwind in the atmospheric boundary layer and descend downwind on return—the “dynamic soaring rule.”⁵ Mathematically, this can be expressed by

$$\begin{aligned}-\pi/2 < \psi < \pi/2 &\Rightarrow \gamma > 0 \\ \pi/2 < \psi < 3\pi/2 &\Rightarrow \gamma < 0\end{aligned}\tag{8}$$

These equations of motion are solved for a family of prescribed trajectories to gain insight relating sailplane parameters to dynamic soaring performance. The prescribed trajectories used here are those parameterized by Barnes and structured such that the aforementioned dynamic soaring rule is enforced. To this end, the flight path angle γ is related to the heading angle ψ through a series of convenient transformations, each operating on the previous one, viz

$$\begin{aligned}\psi_1 &= \psi + \frac{\pi}{2} \\ \psi_2 &= 2\pi \left[\frac{\psi_1}{2\pi} - \text{int} \left(\frac{\psi_1}{2\pi} \right) \right] \\ \psi_3 &= \pi \left[1 - \cos \left(\frac{\psi}{2} \right) \right]\end{aligned}\tag{9}$$

$$\gamma = \gamma_1 \sin \psi_3 + \gamma_2 \sin \psi_3\tag{10}$$

The expressions given in Eq. (9) are shown graphically in Fig. 2. As seen in the last equation, γ_1 defines the maximum possible value for the flight path angle along the orbit. Thus, γ_1 has significant physical influence on the trajectory, and its effects will be explored later in Section IV. The parameter γ_2 is used to “squash” the orbit causing the lower part of the trajectory to flatten near the ground. This trajectory “squash” causes the aircraft to spend more time near the ground, and thereby in Barnes’ case it causes the albatross trajectory model to skim the surface for a longer period of time and simulate albatross feeding behavior on the wing. Finally, the orbit begins above the surface at a prescribed height, which is called here the dwell height z_D .

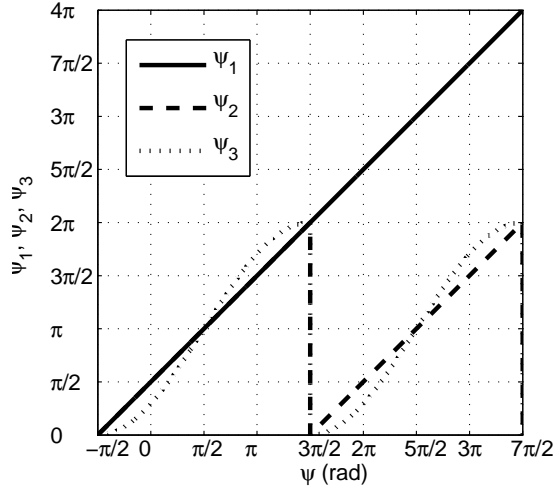


Figure 2. Illustration of parameters used in transformation to define trajectory heading (2 cycles shown).

B. Wind Shear Model

The wind shear in the atmospheric boundary layer has a significant impact on dynamic soaring performance. It is the shear that the airplane uses to gain energy when following a favorable dynamic soaring trajectory. Thus, an accurate model of the wind profile is needed. A logarithmic profile was chosen as this is most applicable to measurements near the surface of the earth.²² The logarithmic profile used is given by

$$U(z) = U_{ref} \frac{\log(z/z_0)}{\log(z_{ref}/z_0)} \quad (11)$$

where $U(z)$ is the wind speed at height z , and U_{ref} is the wind speed at the reference height z_{ref} . The variable z_0 is the aerodynamic roughness length or the roughness factor. It is an experimentally derived constant that accounts for the kind of surface over which the wind is blowing. Typically, a higher value of the roughness length indicates more obstructions on the surface such as trees and buildings. Figure 3 shows wind profiles for three values of the roughness coefficient with $U_{ref} = 13.20$ m/s (29.5 mph) and $z_{ref} = 1.83$ m (6 ft). The value for the reference height z_{ref} was chosen based on the fact that most RC sailplane pilots judge the wind speed at approximately eye level. The value for the reference wind speed is used later to illustrate dynamic soaring over windy open fields.

As noted in Ref. 22, wind profiles over open fields are matched well by a roughness factor of $z_0 = 0.05$ m, which is the value used throughout the remainder of this paper. Figure 4 shows wind profiles for three values of the the reference wind speed with $z_0 = 0.05$ m and $z_{ref} = 1.83$ m (6 ft). These speeds referenced to a height z_{ref} of 1.83 m are correlated with the common reference heights of 10 and 20 m in Table 1 for reference. For instance, a wind profile defined by $U_{ref} = 15$ m/s at $z_{ref} = 1.83$ m corresponds to values of $U_{ref} = 22.080$ m/s at $z_{ref} = 10$ m and $U_{ref} = 24.969$ m/s at $z_{ref} = 20$ m. While a reference wind speed of 20 m/s (44.7 mph) and above becomes extreme, sustained winds in the range 10 and 15 m/s (22.4 to 33.6 mph) are not uncommon. For instance, Table 2 shows sustained winds averaging near ≈ 15 m/s (33.6 mph) at Willard Airport, Champaign, IL²³ on a specific day.

C. Numerical Solution Methodology

These equations of motion together with the system model that included the airplane, wind profile, and defined trajectory are solved iteratively as outlined in the flowchart shown in Fig. 5. In the method, an orbit is defined as starting at the dwell height z_D in a banked turn, climbing into the wind to maximum height, then diving back downwind to the dwell height, albeit at some distance downwind relative to where it began. The entire formulation is framed around making the reference wind speed U_{ref} the dependent quantity such

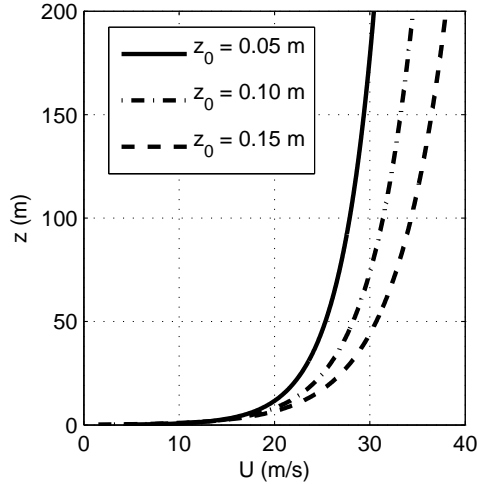


Figure 3. Wind profiles for various roughness lengths ($U_{ref} = 13.20$ m/s and $z_{ref} = 1.83$ m).

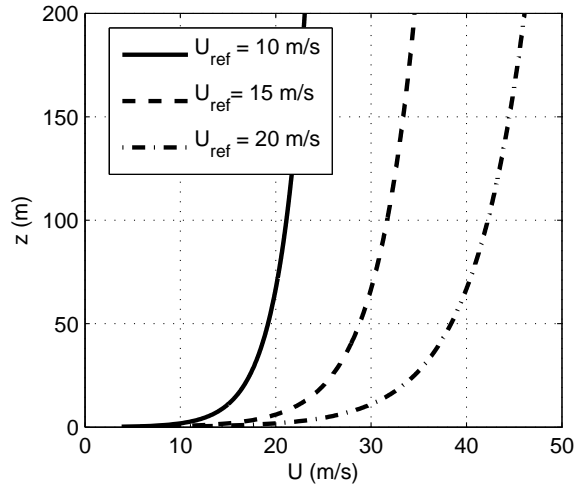


Figure 4. Wind profiles for various reference wind speeds ($z_0 = 0.05$ m and $z_{ref} = 1.83$ m).

that an energy conserving orbit is produced. Thus, the code iterates on the reference wind speed U_{ref} until an energy conserving orbit is obtained, that is, until the energy is the same at the orbit initial and final conditions. This primary orbit solver was included in a “wrapper” code that allowed for simultaneous sweeps on two parameters, with mass always being one of the parameters. Many parameter sweeps were performed with the code, and these results are discussed later in Section IV.

Table 1. Current Wind Profile Reference Values (first line) and Corresponding Values for Standard 10- and 20-m Reference Heights.

z_{ref} (m)	U_{ref} (m/s)		
1.83	10	15	20
10	14.72	22.08	29.44
20	16.65	24.97	33.29

The method was validated against results from Barnes,⁵ in particular the “circular zoom” albatross case reported therein. For this particular case, the prescribed orbit trajectory produces a circular ground trace in the moving vehicle (albatross) frame of reference. Thus, if there were no wind, the prescribed trajectory ground trace would be a circle, thereby having a constant aircraft-relative turn radius.

The physical parameters used to model an albatross are defined as in Table 3. The specific wind model used by Barnes⁵ is an exponential wind profile rather than the one used in the current results [see Eq. (11)]. For the Barnes wind model, the wind speed U at height z is given by

$$v = \frac{U}{U_{ref}} = 1 - e^{-a\zeta} \quad (12)$$

$$\zeta = \frac{z}{z_{ref}}$$

where again the reference wind speed U_{ref} is given at the reference height z_{ref} . The parameter a defines the amount of wind shear. The specific values used are given by

$$\begin{aligned} z_{ref} &= 20 \text{ m} \\ U_{ref} &= 7 \text{ m/s} \\ a &= 7 \end{aligned} \quad (13)$$

Finally, the initial conditions are defined by these dwell conditions:

$$\begin{aligned} V_D &= 25 \text{ m/s}; \psi_D = -\pi/2; \gamma_D = 0 \\ z_D &= 1.8 \text{ m}; x_D = 0; y_D = 0 \end{aligned} \quad (14)$$

The defining trajectory coefficients γ_1 and γ_2 are given by

$$\gamma_1 = \frac{\pi}{15} \text{ (12 deg)}; \gamma_2 = 0 \quad (15)$$

and the aircraft-relative turn radius r for the trajectory was set at 40 m – a constant.

The code runs with all of these parameters as input, iterates on U_{ref} to find the energy-conserving orbit (if one exists), and then saves the final 3D trajectory, resulting U_{ref} , and the orbit time history for one cycle. Figure 6 is the three-dimensional depiction of the orbit as seen by an inertial observer. In this graphic, a airplane representing the albatross is drawn with a wingspan five times that of the albatross. To give a sense of speed, the airplane is drawn every 3 sec along the trajectory. Figure 7 shows the model albatross state characteristics as a function of heading ψ (as a surrogate for time). These results match the same case presented by Barnes.

Table 2. Wind Conditions at Willard Airport, Champaign, IL on April 29, 2010 at 10-m Height.²³

Time	Winds	Speed	Gusts	Vis.	Temp.	Rel. Humidity
		m/s (mph)	m/s (mph)	km (mi)	deg F	%
9:53 AM	S	13.86 (31)	17.43 (39)	16.09 (10)	66	43
10:53 AM	S	13.86 (31)	17.89 (40)	16.09 (10)	72	37
11:53 AM	S	14.76 (33)	18.33 (41)	16.09 (10)	73	36
12:53 PM	S	16.55 (37)	20.56 (46)	16.09 (10)	75	36
1:53 PM	S	14.76 (33)	23.47 (52)	16.09 (10)	77	36
2:53 PM	S	15.65 (35)	21.46 (48)	16.09 (10)	77	36
3:53 PM	S	15.20 (34)	21.01 (47)	16.09 (10)	79	36
4:53 PM	S	15.65 (35)	20.56 (46)	16.09 (10)	79	36
6:53 PM	S	15.65 (35)	19.67 (44)	16.09 (10)	73	36
7:53 PM	S	9.38 (21)	13.86 (31)	16.09 (10)	70	36

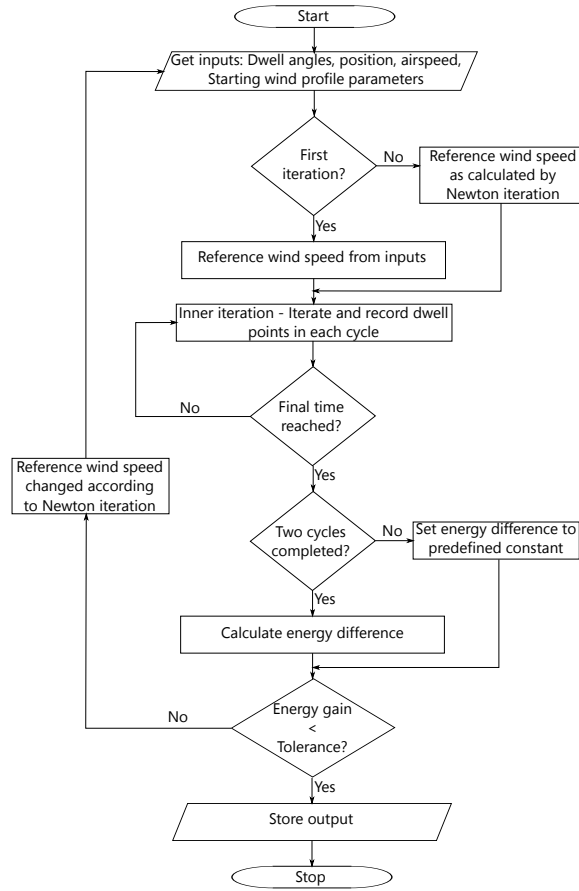


Figure 5. Flowchart illustrating method to find energy conserving orbit.

Briefly, Fig. 6 shows the resulting trajectory starting at the dwell conditions. At this particular moment, the albatross is flying crosswind before turning and climbing upwind. From the peak, the albatross flies downwind to a point further downwind than where it began. As Fig. 7 shows, the maximum airspeed V is near 25 m/s (55.9 mph) at the dwell condition. Interestingly, throughout the orbit, the total energy (energy height h_e) and lift-to-drag ratio L/D stay nearly constant. The load factor n reaches a peak near 2 before dwell height and then unloads to a value of 1 at peak altitude. In maintaining near constant total energy, the balance between kinetic energy (wind relative) and height is clearly seen. The distance from start-to-finish is 69.8 m, taking 11.8 sec for an average downwind transit speed of 5.9 m/s (13.2 mph).

Table 3. Albatross Physical Characteristics for Modeling Dynamic Soaring.⁵

Parameter	Value
m	11 kg (24.25 lb)
m/S (W/S)	14.37 kg/m ² (47.08 oz/ft ²)
b	3.5 m (11.5 ft)
AR	16
e	0.9
C_{D_0}	0.015
$(L/D)_{max}$	27.46

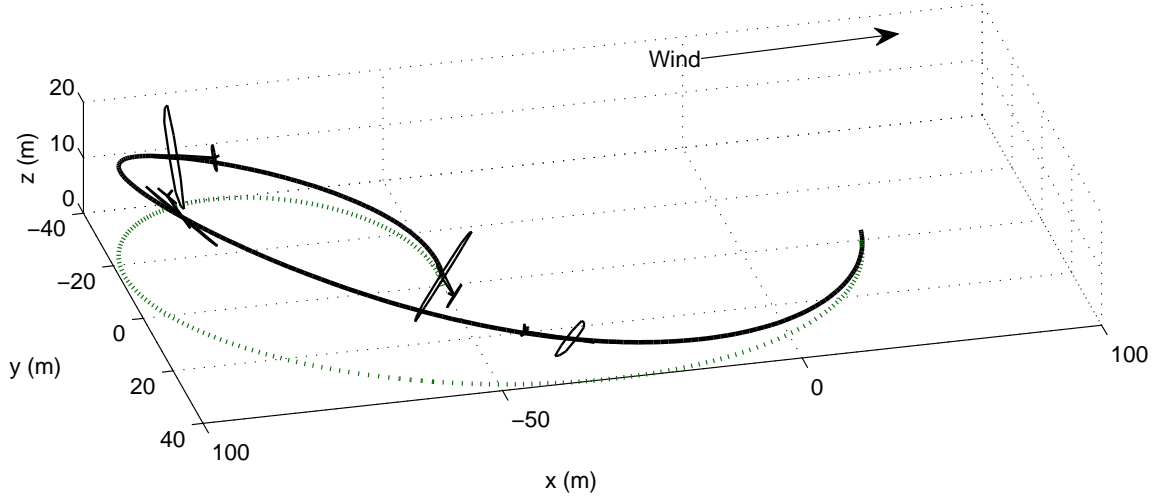


Figure 6. Trajectory of an albatross performing dynamic soaring (aircraft model magnified 5 times normal size and drawn every 3 sec).

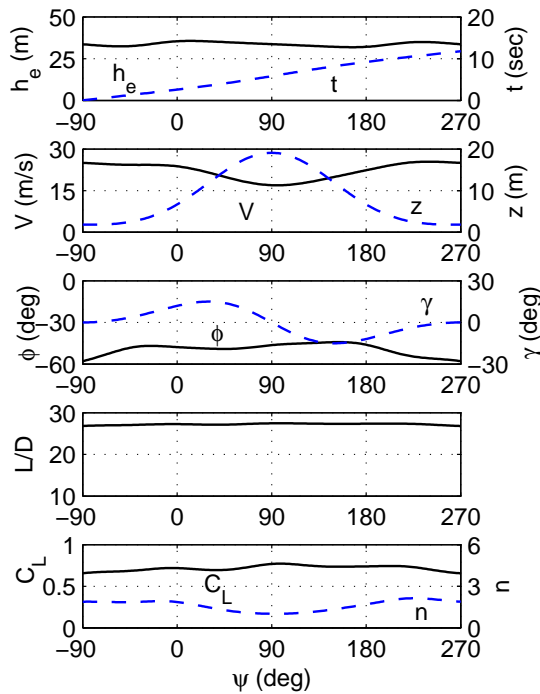


Figure 7. Albatross dynamic soaring orbit parameters for one orbit (see Fig. 6).

III. High-Altitude Dynamic Soaring – Baseline Case

The objective of this study was to investigate the feasibility of attaining high altitudes over open fields using dynamic soaring. A large parameter space was explored to define a baseline that ultimately achieved a high altitude of 185.1 m (607.3 ft). This exploratory process was based in part on experience gleaned while using a piloted realtime flight simulator discussed in Section V. The properties of the resulting sailplane, having a 3-m wingspan, are given in Table 4. It is representative of rather typical dynamic soaring capable sailplanes that are generally characterized by both high wing loadings and high maximum lift-to-drag ratios.

In defining the baseline orbit, practical considerations were taken into account in setting the dwell conditions. Flying in the strongest wind shear close to the ground is beneficial in dynamic soaring, but piloting skills must be considered. Experience has shown that ≈ 2 -m ground clearance offers a skilled competition-level pilot enough margin for error in maneuvering at the high zoom speeds near ground under a variety of conditions. With these factors in mind, a conservative dwell height of 5 m was used. This height is the position of the aircraft center of gravity, yielding a tip clearance of 3.5 m for the 3-m wingspan baseline sailplane. The dwell speed was set at 65 m/s (145 mph) which is well within the capabilities of pilots having experience with dynamic soaring conditions over mountain ridges. Thus, the dwell conditions (initial conditions) for the prescribed orbit are

$$\begin{aligned} V_D &= 65 \text{ m/s}; \psi_D = -\pi/2; \gamma_D = 0 \\ z_D &= 5 \text{ m}; x_D = 0; y_D = 0 \end{aligned} \quad (16)$$

The additional trajectory coefficients γ_1 and γ_2 were selected to be

$$\gamma_1 = 0.9 \text{ (51.6 deg)}; \gamma_2 = 0 \quad (17)$$

The high value for the flight path angle parameter γ_1 causes the aircraft to experience high wind shear which increases the dynamic soaring thrust and aid in the achievement of a high orbit [see Eq. (3)]. For this case, the airplane-relative circular turn radius r was set at 100 m. The wind profile model is that defined previously by Eq. (11) with the values of the roughness coefficient and reference height given by

$$\begin{aligned} z_{ref} &= 1.83 \text{ m} \\ z_0 &= 0.05 \text{ m} \end{aligned} \quad (18)$$

Newton iteration was used to solve for the required reference wind speed that yielded an energy conserving orbit for the conditions prescribed. The resulting reference wind speed U_{ref} was found to be 13.20 m/s as represented previously in Fig. 3.

The resulting dynamic soaring orbit and orbit parameters through one cycle are shown in Figs. 8 and 9. As seen the altitude is extreme (reaching a height of 185.1 m). The 200-m orbit width is consistent with the prescribed 100-m radius orbit. The aircraft travels a net downwind distance of 445 m over a period of 16.2 sec, giving an average downwind travel speed of 27.5 m/s (61.5 mph). Throughout the entire cycle, the sailplane must in effect crab into the wind, which accounts for the odd looking orientation of the aircraft relative to the flight path trajectory. From the view angle used to render Fig. 8, the crab is most apparent near the point of maximum height.

Comparing orbit parameters through one cycle shown in Fig. 9 with the Barnes case in Fig. 7, it can be seen that the lift coefficient is lower than that for the albatross case, which is in part due to the fact that the aircraft is flying at higher speed. The bank angle is higher, resulting from the high speeds and radius of curvature required which together result in a higher load factor. Overall the lift-to-drag ratio, load factor and all others show greater variation than for the albatross case. The load factor peaks near 6 at the end of the cycle while turning away from the ground to repeat the cycle. Clearly the high load factor and high speed combined are reasons why dynamic soaring orbits such as this are not observed in nature. From a practical

Table 4. Baseline Sailplane Characteristics for High-Altitude Dynamic Soaring

Parameter	Value
m	15 kg (33.07 lb)
m/S (W/S)	33.33 kg/m ² (109.23 oz/ft ²)
b	3 m (9.58 ft)
AR	20
e	0.9
C_{D_0}	0.020
$(L/D)_{max}$	26.59

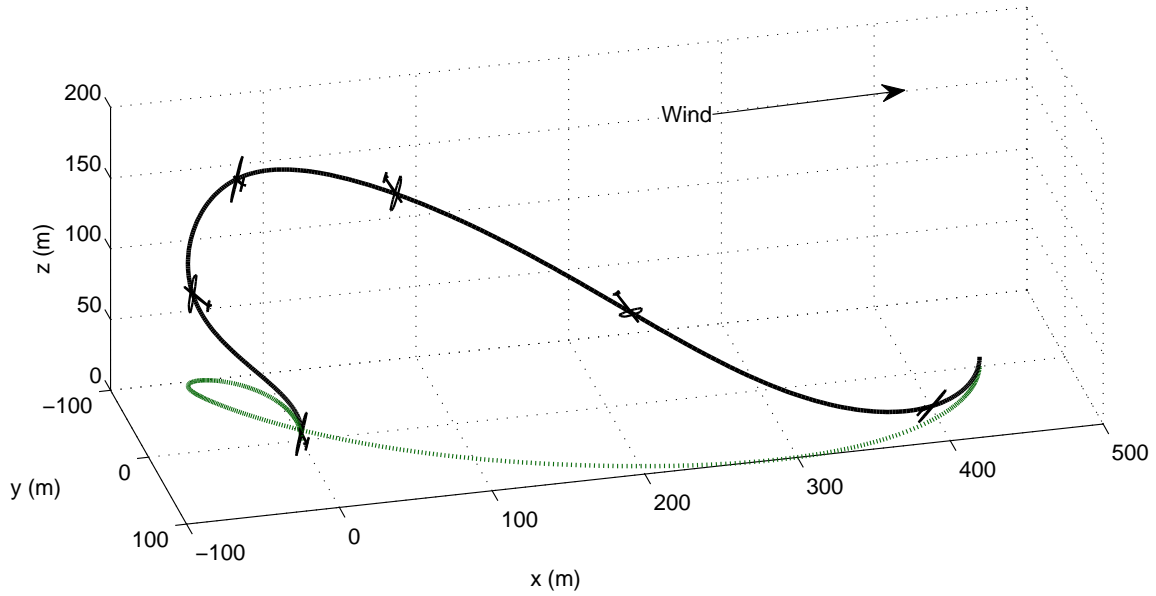


Figure 8. Sailplane trajectory for high-altitude dynamic soaring (sailplane model magnified 10 times normal size and drawn every 3 sec).

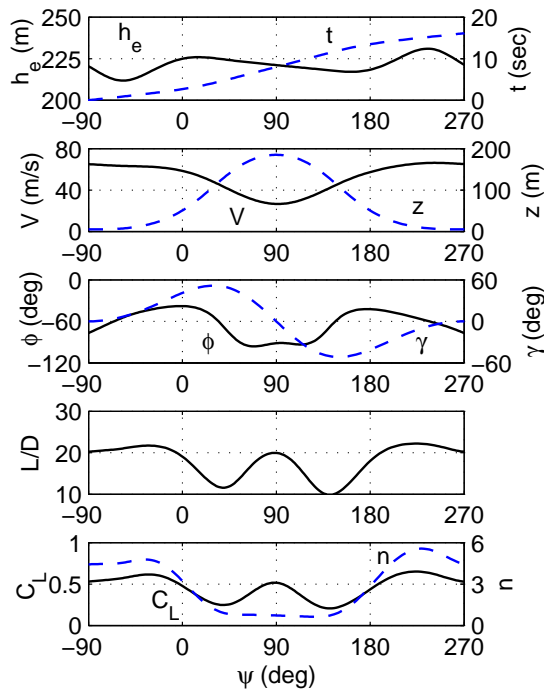


Figure 9. High-altitude dynamic soaring orbit parameters for one cycle (see Fig. 8).

standpoint, however, the trajectory and physical characteristics along the path are not extraordinary, apart from the unexpectedly high altitude achieved.

IV. Parameter Sweeps

In this section, parameter sweeps around the previous baseline are performed to explore the design space that can give rise to high-altitude dynamic soaring. The baseline values and the sweep ranges for the individual parameters are shown in Table 5. The aircraft and orbit parameters used in the previous high-altitude dynamic soaring case are included in every sweep case. The sweep ranges for individual parameters were chosen so as to encompass a wide range to better define and outline the feasible design space. Two-parameter sweeps were performed with mass always being one and the other (see Table 5) was selected in turn from the following: aspect ratio, parasite drag coefficient, dwell speed, dwell height, orbit flight path angle parameter, and orbit radius. The latter three affect the final orbit altitude because they define the trajectory relative to the aircraft, while for the others the maximum orbit height is set by the baseline values yielding the maximum height of 185.1 m for an orbit starting at the baseline dwell height of 5 m. For all cases, the wing planform efficiency was fixed at the baseline value ($e = 0.9$).

As before, the numerical solution was framed to yield the required reference wind speed giving rise to energy-conserving dynamic soaring orbits. Thus, the reference wind speed is the primary dependent quantity of interest in all cases. In the graphics presented, the reference wind speed U_{ref} scale was stopped at 25 m/s because speeds in this range and above are rarely attained over open fields in conditions amenable to piloted dynamic soaring. In cases where the orbit changes, the maximum altitude is also a dependent quantity, and this data is presented as well.

It is worth mentioning that for all orbits in this section (and before) the aircraft stays within the boundary layer. Also, in cases where an increase or decrease of a baseline parameter resulted in a physically unrealizable energy-conserving orbit, the baseline parameter was chosen as the upper or lower bound for that sweep case. These baseline-bounded sweep cases correspond to those with ‘-’ given in Table 5.

A. Effects of Aircraft Properties

Figures 10–12 show the required reference wind speed for changing aircraft mass along with span, aspect ratio, and parasite drag coefficient, respectively. In all figures, the baseline case is shown for comparison by a single circle symbol. What is immediately clear is that increasing mass lowers the required wind speed for sustaining energy-conserving dynamic soaring orbits. In fact, as all trends indicate, the mass of the baseline case is the most favorable, and clearly a higher mass would further reduce the required wind speed.

The effect of higher mass is consistent with prior studies indicating that high wing loading is beneficial to dynamic soaring performance. The reason for this relates back to Fig. 1 which shows the main driver behind dynamic soaring thrust. The longer a sailplane can penetrate into the wind, the more time there is for dynamic soaring thrust to be produced and thereby increase the aircraft energy and sustain the perpetual orbit. Thus, sailplanes with higher mass (higher wing loading) are able to more efficiently sustain the condition (penetration into the wind) that gives rise to dynamic soaring thrust.

In each of these cases, the trajectory “schedule” is the same, that is, the flight path angle along the orbit as a function of heading ψ is the same, and also the circular orbit relative to the aircraft is the same ($r = 100$ m). Consequently, the maximum height of the orbits is constant and same as the baseline (185.1 m),

Table 5. Baseline and Lower/Upper Bounds for Aircraft and Trajectory Parameters

Parameter	Lower Bound	Baseline	Upper Bound
m (kg)	6	15	-
b (m)	-	3	4.2
AR	15	20	25
C_{D_0}	0.015	0.020	0.025
V_D (m/s)	-	65	80
z_D (m)	3	5	8
γ_1	0.4 (22.9 deg)	0.9 (51.6 deg)	-
r (m)	60	100	110

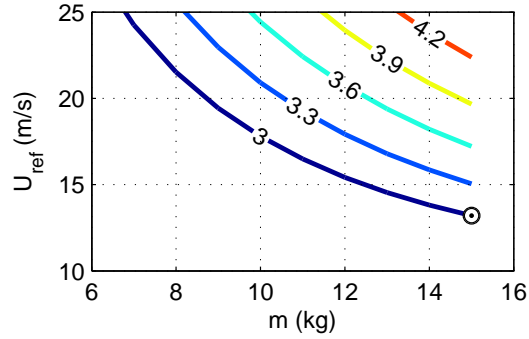


Figure 10. Dynamic soaring reference wind speed as a function of sailplane mass for various wingspans b ranging from 3 to 4.2 m (baseline case shown as circle symbol).

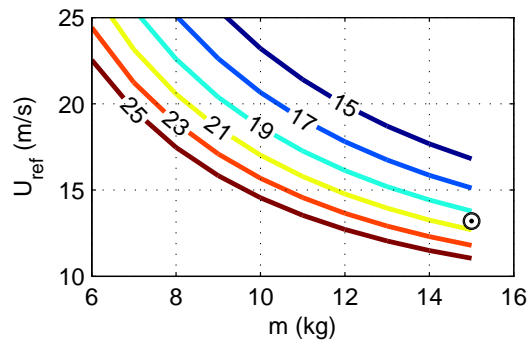


Figure 11. Dynamic soaring reference wind speed as a function of sailplane mass for wing aspect ratios AR ranging from 15 to 25 (baseline case shown as circle symbol).

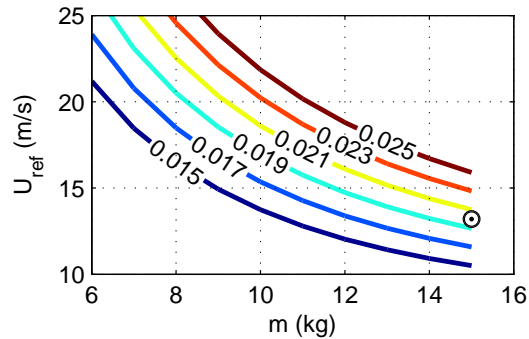


Figure 12. Dynamic soaring reference wind speed as a function of sailplane mass for various C_{D_0} values (baseline case shown as circle symbol).

and the width of the orbit is constant (200 m) for all data represented in Figs. 10–12. Since the higher wing loading cases all trend toward requiring less wind to achieve the same maximum altitude of 185.1 m, they are said here to be more “efficient.” Thus, reference here to higher efficiency relates to a lower required wind speed to sustain dynamic soaring.

The effects of sailplane span shown in Fig. 10 are a direct result of changes in wing loading. For a given aircraft mass, decreasing the span with fix aspect ratio ($AR = 20$) results in lower wing area and consequently higher wing loading. The trends show that a span smaller than the baseline would be even more efficient. It must be considered, however, that a smaller span would correspond to a smaller airplane with what might

become an exceptional high weight. At some point with such a high wing loading managing to launch and land such an airplane could prove to be one of the largest challenges to successful extreme-orbit dynamic soaring.

Figure 11 shows the effects of changing aspect ratio with all else constant except for changing mass as the second parameter. The result is clear that higher aspect ratios yield higher values for $(L/D)_{max}$. Consequently, with higher aspect ratios less energy is lost due to drag and thus dynamic soaring becomes more efficient with a lower required wind speed. For reference, as shown in Table 6 the $(L/D)_{max}$ ranges from approximately 23 to 30 for aspect ratios of 15 to 25, respectively.

Lowering the parasite drag coefficient C_{D_0} as shown in Fig. 12 produces results similar to those for increasing aspect ratio because of the direct effect on improving $(L/D)_{max}$. As Fig. 12 shows, a sailplane configured like the baseline but with $C_{D_0} = 0.015$ yields a reference wind speed near 10 m/s. For the standard height of $z_{ref} = 10$ m, the corresponding reference wind speed is 14.72 m/s (see Table 1), which nearly matches the example weather case presented in Table 2. The value $C_{D_0} = 0.015$ is reasonable for a high-performance model-scale sailplane. For reference, as shown in Table 7 the $(L/D)_{max}$ ranges from approximately 24 to 31 for parasite drag coefficients of 0.025 to 0.015, respectively.

For all cases, the maximum load factor was between approximately 5 and 7 and occurred near $\psi \approx 225$ deg (similar to that shown in Fig. 9). Also this point corresponds to the highest airspeed which was between approximately 66 and 71 m/s for all cases (with the maximum being 70.89 m/s corresponding to the case in Fig. 10 with $m = 15$ kg and $b = 4.5$ m).

B. Effect of Initial Condition – Dwell Speed

Figure 13 shows the effects of changing the dwell speed, which is the initial orbit speed. As before, all other parameters are held constant apart from sweeping mass. Generally, a higher dwell speed increases the speed around the entire orbit, and to sustain this higher speed more wind shear is required. Consequently a higher reference wind speed results from increasing the dwell speed as shown in Fig. 13. At a dwell speed much below 65 m/s, the solution for the highest mass does not converge because near the maximum height the airspeed slows to a point lower than stall speed.

C. Effects of Trajectory Parameters

The three main trajectory parameters are the initial height z_D , flight path parameter γ_1 , and orbit radius r . With all else fixed, z_D as the direct effect of increasing the maximum altitude because it merely shifts the entire orbit up by the increment in z_D based simply on the fixed orbit shape defined by r and γ_1 . However, moving the orbit up makes it less efficient because the sailplane does not benefit as much from the stronger wind shear near the surface. This resulting effect on efficiency is clearly shown in Fig. 14, and Fig. 15 shows the simple one-for-one result of incremental higher maximum altitude with each increment in dwell height. It is worth noting that a dwell height of 3 m gives a wing tip clearance approaching 1.5 m, which is most likely beyond the skills of a pilot to manage reliably.

The effect of changing the flight path angle parameter is shown in Fig. 16. An increase in this parameter γ_1 causes the flight path angle to increase around the entire orbit, making it more inclined to the wind. As

Table 6. Maximum Lift-to-Drag Ratio for Various Aspect Ratios

AR	15	17	19	20	21	23	25
$(L/D)_{max}$	23.02	24.51	25.91	26.59	27.24	28.51	29.72

Table 7. Maximum Lift-to-Drag Ratio for Various C_{D_0} Values

C_{D_0}	0.015	0.017	0.019	0.020	0.021	0.023	0.025
$(L/D)_{max}$	30.70	28.84	27.28	26.59	25.95	24.79	23.78

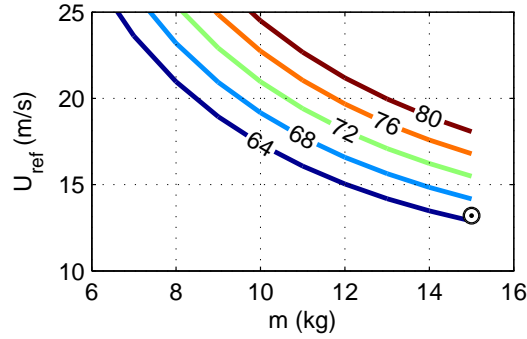


Figure 13. Dynamic soaring reference wind speed as a function of sailplane mass for various dwell speeds ranging from 64 to 80 m/s (baseline case shown as circle symbol).

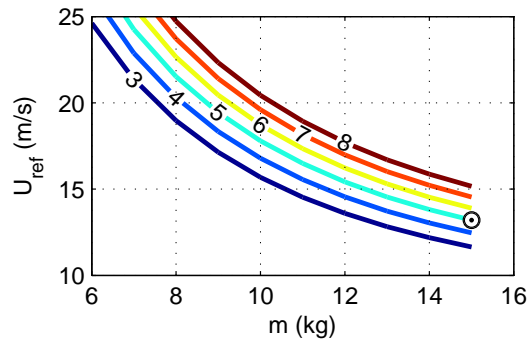


Figure 14. Dynamic soaring reference wind speed as a function of sailplane mass for various dwell heights ranging from 3 to 8 m (baseline case shown as circle symbol).

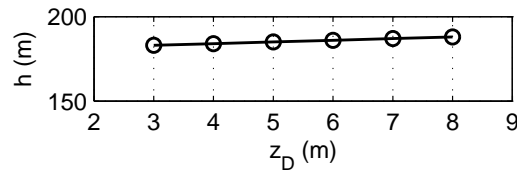


Figure 15. Orbit maximum height with increasing dwell height z_D showing one-for-one correspondence.

this orbit becomes more inclined, the maximum height is increased based on simply the geometry of the orbit, and this result is shown in Fig. 17. The baseline is the bounding case for which the maximum altitude is 185.1 m, and from the results shown in Fig. 16 a further increase in the inclination of the orbit would not make it more efficient, i.e. it appears that the point of diminishing returns has been nearly reached with a minimum reference wind speed of 13.20 m/s (see Fig. 16) corresponding to the baseline case. With the dwell speed fixed for this two-parameter sweep, it is not surprising to find that for all cases the maximum speed is between 66 and 68 m/s near $\psi \approx 225$ deg. The maximum load factor stays between approximately 5 and 6.

Changes in the orbit radius are shown in Fig. 18. The orbit radius, as mentioned before, is the radius of the ground trace of the orbit that the aircraft “sees” itself flying. For the fixed flight path angle schedule [see Eq. (10)], a larger radius magnifies the orbit size which results in a higher maximum orbit altitude as shown in Fig. 19. As expected with the maximum speed set mainly by the dwell speed, the load factor in this case was driven by the radius. In particular, with these changes in radius, the maximum load for the 6-kg case changed from 9.2 to 5.6 for radii of 60 to 110 m, respectively. Correspondingly, for the 15-kg case,

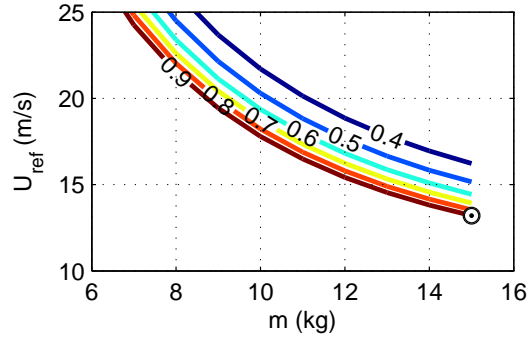


Figure 16. Dynamic soaring reference wind speed as a function of sailplane mass for various γ_1 values ranging from 0.4 (22.9 deg) to 0.9 (51.6 deg) (baseline case shown as circle symbol).

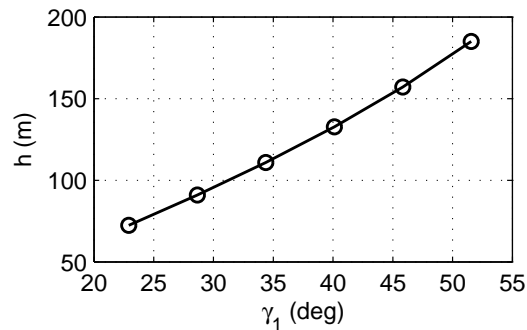


Figure 17. Orbit maximum height with increasing orbit γ_1 .

the load factor peaked at 5.6 to 5.1 for radii of 60 to 110 m.

The trend shown in Fig. 18 departs from that discussed so far. For mass on the lower side of the range, say, $m = 8$ kg, the orbit with the larger radius reaching a higher altitude (Fig. 19) requires a higher reference wind speed, but this same trend does not occur on the upper bound with $m = 15$ kg where the reference wind speed is approximately the same for any radii (any maximum height). Beyond this point (not shown) the curves cross over with the higher radius case becoming the most efficient. Or put somewhat differently, there appears a minimum for each curve, each in turn. This minimum point (which results in overlapping curves¹⁹) happens as a result of the tradeoff between parasite drag and induced drag. For the 60-m radius case (or any case for that matter), dynamic soaring is less efficient at lighter wing loadings (lower mass) because of high parasite drag; whereas, at higher wing loadings it is less efficient because of high induced drag (with induced drag being proportional to span loading). At some point between having either high parasite drag or high induced drag there is a minimum required reference wind speed, which corresponds to the minimum required shear that has been the subject of numerous other investigations on dynamic soaring, e.g. Refs. 4 and 6.

D. All Favorable Characteristics Combined

Based on the trends within the ranges considered, the most favorable case is given in Table 8. For dynamic soaring over the full extent of the boundary layer (185.1 m), a reference wind speed of 8.81 m/s (19.07 mph) is required, and using Table 1 this corresponds to winds below those actual conditions given in Table 2. At these conditions with the dwell speed of 65 m/s, the wing chord average Reynolds number ranges from $\approx 200,000$ near peak altitude to $\approx 530,000$ at the dwell conditions. Moreover, the lift coefficient ranges from 0.16 to 1.12 from dwell to maximum altitude.

Table 8. Favorable Sailplane Characteristics for High-Altitude Dynamic Soaring

Parameter	Value
m	15 kg (33.07 lb)
m/S (W/S)	41.67 kg/m ² (136.54 oz/ft ²)
b	3 m (9.58 ft)
AR	25
e	0.9
C_{D_0}	0.015
$(L/D)_{max}$	34.32

V. Piloted Dynamic Soaring Simulation

High-altitude dynamic soaring that resembles the prescribed trajectories previously discussed was simulated in a piloted realtime flight simulator. In the simulator, the full 6-DOF equations of motion are solved using quaternions, and integration is carried out using a Runge-Kutta 4-th order scheme running at 300 Hz on a desktop PC. The aerodynamics are modeled based on a component build-up approach using table lookup for aerodynamic coefficients as functions of angle of attack, control surface deflections, etc. Table lookup is also used for the vertical wind profile, with the particular wind profile shown in Fig. 20 which was constructed from a composite of near-ground measurements²⁴ and a standard power law winds-aloft model.²⁵ For the reference height $z_{ref} = 1.83$ m, $U_{ref} = 13.45$ m/s for this profile. At other heights, the

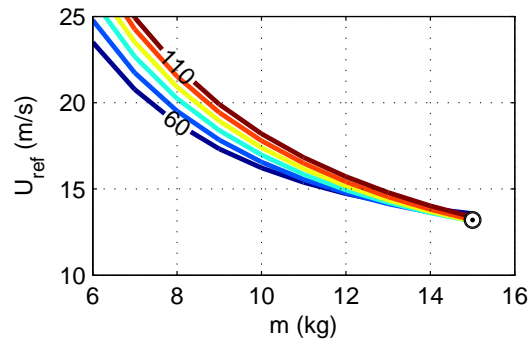


Figure 18. Dynamic soaring reference wind speed as a function of sailplane mass for various orbit radii ranging from 60 to 110 m (baseline case shown as circle symbol).

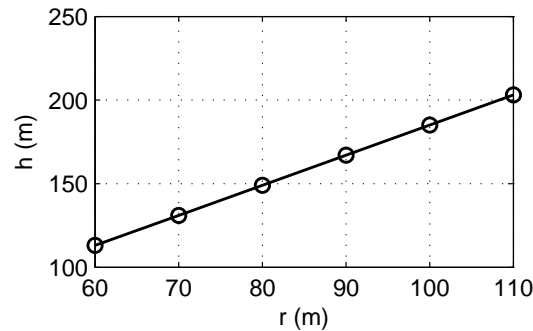


Figure 19. Orbit maximum height with increasing orbit ground radius.

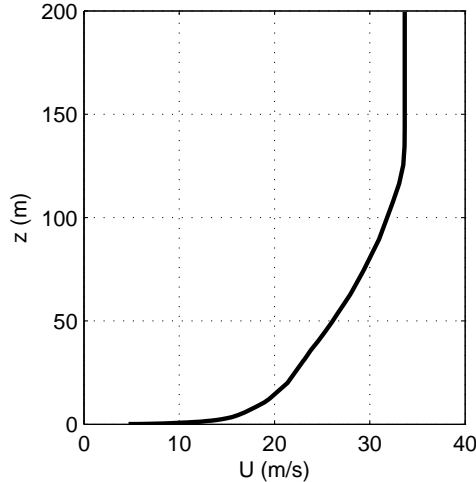


Figure 20. Wind profile used in simulations ($U_{ref} = 13.45$ m/s and $z_{ref} = 1.82$ m).

values are $U(z = 10 \text{ m}) = 18.68$ m/s and $U(z = 20 \text{ m}) = 21.34$ m/s. With this wind profile, wind shear is smoothly terminated at a height of near 125 m. The properties of the sailplane flown in the simulation are given in Table 9. The 4-m wingspan sailplane has characteristics somewhat similar to the previous baseline with a high lift-to-drag ratio and high wing loading (Table 5).

The particular simulator used is the commercial FS One™ RC flight simulator.²⁶ It allows for pilot input through a standard RC transmitter attached to a USB adapter connected to the computer. The simulator includes flight dynamics recording features that allow for saving state data recorded during simulation to a file. The particular recorded flight shown here comes installed with the original software.

Figures 21 and 22 show the trajectory and orbit parameters for one nominal cycle. In this case, the cycle is defined to start and end at $\Delta\psi = -90$ and 270 deg where the absolute initial heading ψ is 78.1 deg. Again the heading, $\Delta\psi$ in this case, is a surrogate time, or pseudo time. The total time for the segment is 11.5 sec over a distance of 399.9 m, making the net downstream travel speed 34.67 m/s (77.6 mph). The flight was flown using a strategy that was found by trial and error to maximize peak altitude *as well as* maximize downwind net travel speed. This flight was flown and recorded in the simulator in year 2006, and it provided in part the motivation for this research.

At a glance, the piloted trajectory appears somewhat different than the scheduled trajectory for the baseline shown in Fig. 8, but for the most part these differences are related to the amount of crab when flying crosswind. The wind speeds aloft for the baseline and piloted flights are similar, but the greatest difference is in the wing loading with the baseline case being much higher. As a result the piloted sailplane cannot penetrate as much into the wind but instead drifts more downwind resulting in a ground trace that shows a cusp (Fig. 21) instead of a loop (Fig. 8).

Because the airplane crabs into the wind by an amount that depends on the wind speed relative to the airspeed, plotting the effective time history vs absolute ψ (that is from $\psi = -90$ to 270 deg) is not the best

Table 9. Sailplane Parameters Used in Realtime Simulation Demonstration

Parameter	Value
m	12 kg (26.45 lb)
m/S (W/S)	12.67 kg/m ² (41.53 oz/ft ²)
b	4 m (13.12 ft)
AR	16.9
$(L/D)_{max}$	≈ 26

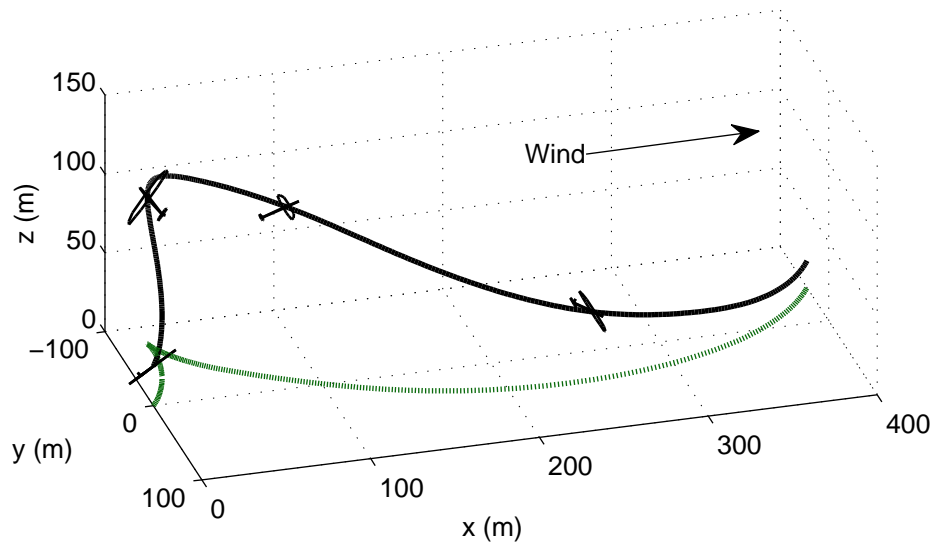


Figure 21. Dynamic soaring trajectory of a 4-m wingspan sailplane flown using the FS One flight simulator (sailplane magnified 10 times normal size and drawn every 3 sec).

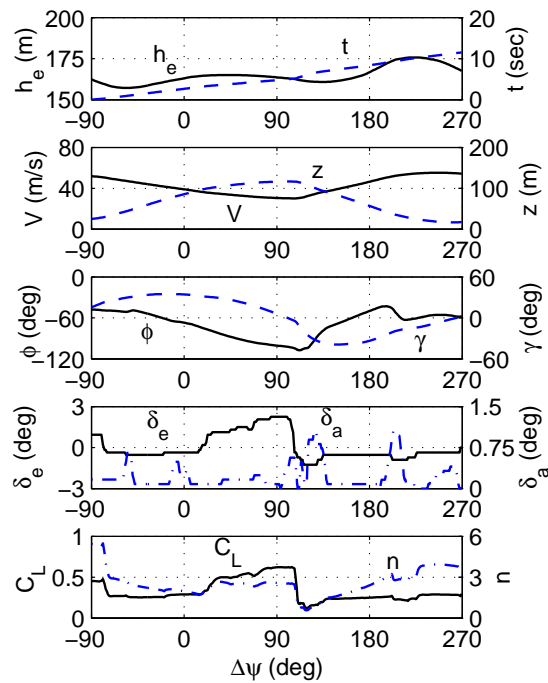


Figure 22. High-altitude dynamic soaring orbit parameters for one nominal cycle during the simulation (see Fig. 21).

point of reference. Instead, the time history has been plotted so that it begins at the dwell condition and ends downstream at the same initial heading, that is, $\Delta\psi = 360$ deg later. This end point is close to but not necessarily the next dwell condition because the flight is piloted and hence not perfectly periodic. As a result, the initial and final conditions are slightly different. Nevertheless, it is clearly one orbit and can be compared with the baseline orbit.

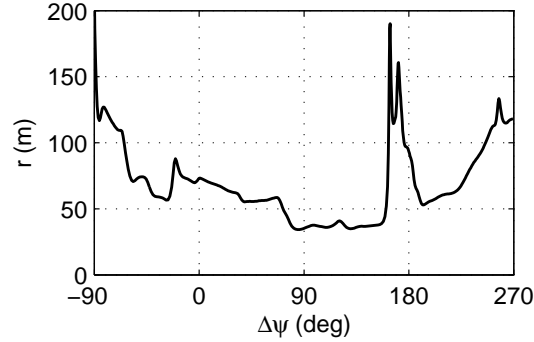


Figure 23. Instantaneous orbit ground radius r computed from time history (see Fig.22).

The altitude reaches a peak near 120 m, which is the point around which the wind shear goes to zero. Thus, without wind shear, there is no possible energy extraction and consequently no possibility for sustaining energy conserving orbits higher than this point. It can be seen from the time history that there is a gain in energy (gain in energy height h_e) that starts near $\Delta\psi \approx -60$ deg as the sailplane turns into the wind and starts to climb. For this period of time, the flight path relative to the ground takes a near vertical climb to the peak, the energy height then begins to plateau and decay before starting to grow again with the downwind zoom near $\Delta\psi \approx 135$ deg. Overall the time history of the energy height is similar to that for the baseline, and this results directly from the tradeoff between speed and height, which are also similar to the baseline.

Not surprisingly with the orbit being similar to the baseline, the time histories for the flight path γ and bank angle ϕ are similar apart from the perturbations that are a direct consequence of the pilot controls. The elevator time history shows a gradual up-elevator command through the climb phase, and the lift coefficient increases as expected. Then upon turning downwind a slight amount of down-elevator command is used and the lift coefficient correspondingly drops (in a fashion that is most likely not optimal in terms of total orbit energy management). The aileron input is slight throughout the entire orbit and pulsed momentarily to a peak near 0.75 deg twice with small pulses given for minor bank angle corrections. Since these inputs are so slight their correspondence with bank angle is mostly imperceptible. Throughout the entire orbit the load factor is modest and appears to be at a peak near 4 corresponding with expected values for elevator input and lift coefficient. As mentioned before the initial and final values for this time history are not equal as is expected with active pilot input.

The flight path angle around the orbit has characteristics similar to that for the baseline scheduled flight path angle (Fig. 9). For the baseline orbit, the turn radius is held fixed; whereas, for the piloted case the turn radius is driven by the pilot commands. Using Eq. (4), the instantaneous turn radius can be computed from the time history, and the result is shown in Fig. 23. For this cycle the average radius is 78.9 m. The spike in radius around $\Delta\psi \approx 180$ deg occurs on the downwind leg. As mentioned, the flight was flown to also maximize downwind travel speed (besides maximizing height), and it was found that “stretching out” the downwind leg increased the downwind travel speed. The increase in radius is a direct indication of the period in time when the trajectory was less curved and directed more downwind.

The single dynamic soaring orbit shown in Fig. 21 was extracted from the full longer flight shown in Fig. 24. The entire trajectory was piloted in realtime using only dynamic soaring to stay aloft. The flight begins at a point where $z = 16$ m (52.5 ft) at an airspeed of 35.4 m/s (79.2 mph). Symbols are drawn every 10 sec to give a sense of speed downwind; however, specifically the full recording shown lasted 244.2 sec over a total distance traveled of 8626 m giving an average downwind speed of 35.32 m/s (79 mph). The single orbit shown in Fig. 8 starts at $x = 3315.4$ m in this larger time history. Figure 25 shows the elevation history for the same flight with symbols again space 10 sec apart.

What can be gleaned from the full flight is that as expected if one orbit can be successfully completed a full continuous series can be completed indefinitely. More importantly, however, it does demonstrate that piloted dynamic soaring over land is likely possible with the right combination of weather, wind, airplane

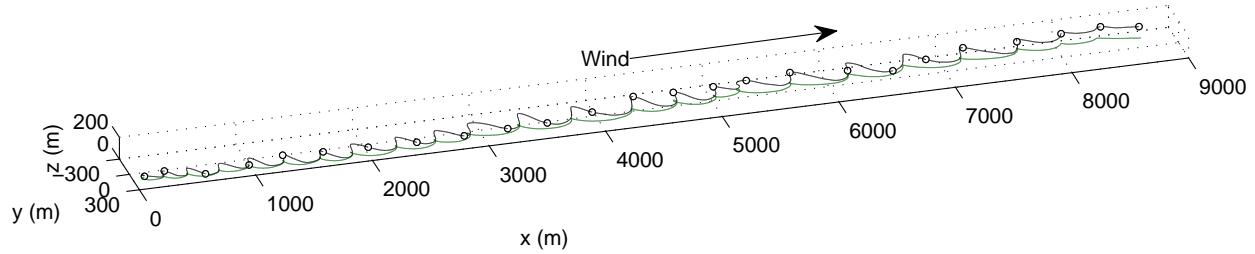


Figure 24. Full 244.2-sec flight that includes the single orbit shown in Fig. 21.

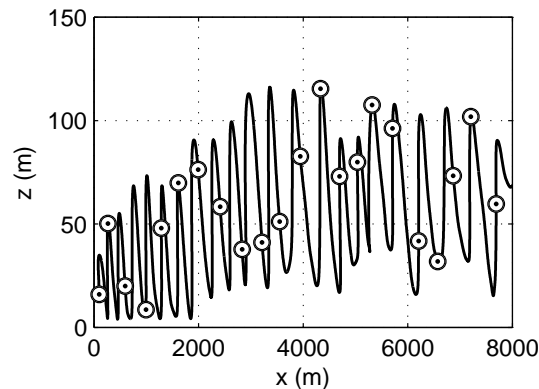


Figure 25. Elevation history of flight shown in Fig. 24.

characteristics, and pilot skills. Another interesting element is that the sustained dynamic soaring does not need to begin from a full larger orbit. As Fig. 25 shows, the peak height of each orbit builds over time from a point with initial conditions that are easily physically realizable. Also, the orbit does not require flying over the full extent of the boundary layer, which is advantageous when one considers that in any long flight like this there will likely be ground obstructions that must be avoided to prevent collisions. Finally, after the orbit has been sustained with near regular periodicity, the elevation fluctuates which illustrates that the trajectory is robust, and thus the trajectory is also likely to be robust to turbulence.

As a final comment, the piloted simulation supports the suggestion that dynamic soaring can be synchronized with the natural phugoid-type motions.³ Using the average airspeeds of 51.5 and 42.4 m/s for the prescribed trajectory baseline orbit (Fig. 8) and the piloted flight (Fig. 21), yields phugoid time periods [$T \approx \pi\sqrt{2}(V/g)$] of 23.34 and 19.20 sec as compared with the actual orbit times of 16.2 and 11.5 sec, respectively. These differences in times between the longitudinal phugoid mode and the “dynamic-soaring phugoid” mode must be related to the non-linear effects of dynamic soaring, that is, wind shear (energy extraction), large angle of attack changes, and the fact that dynamic soaring involves turning. The common denominators between longitudinal-flight phugoid and the “dynamic-soaring phugoid” are the following: 1) both involve a tradeoff between kinetic energy and potential energy, 2) both happen over a relatively long period, and 3) both require no input from the pilot. To elaborate on the latter point, it was found to be easy in the simulator to perform piloted dynamic soaring in the atmospheric boundary layer because over a period of time the sailplane could be “trimmed” to fly the orbits in what seemed like synchronization between the dynamic soaring orbit and the “dynamic-soaring phugoid” with only minuscule (“no”) pilot corrections required.

VI. Conclusions

Based on the results presented in this paper, extreme dynamic soaring to high altitudes over open land in high (realistic) wind conditions appears feasible. Both a point-mass prescribed trajectory simulation and a 6-DOF piloted simulation show that the achievement of dynamic soaring from the ground to near the edge of the atmospheric boundary layer (where the wind shear approaches zero) is an extension of the type of dynamic soaring performed by the albatross. Significant differences are, however, higher airspeeds required (65 m/s) and high load factors (6 to 9). Reference wind speeds between approximately 15–20 m/s (for $z_{ref} = 10$ m) are required for sailplanes with wingspans near 3 m with wing loadings in the range ≈ 12 –30 kg/m² depending on the amount of wind shear. For such conditions, energy-conserving dynamic soaring orbits from ground level to 120–180 m in wind shear appear possible. Finally, flight under these conditions requires little pilot workload with only minor pilot inputs required to maintain consistent and robust high-energy dynamic-soaring orbits over land.

References

- ¹Rayleigh, L., “The Soaring of Birds,” *Nature*, Vol. 27, 1883, pp. 534–535.
- ²Hendriks, F., *Dynamic Soaring*, Ph.D. thesis, University of California, Los Angeles, CA, 1972.
- ³Hendriks, F., “Extraction of Flow Energy by Gliding in a Wind with Uniform Vertical Shear,” University of California, UCLA-ENG-7324, Los Angeles, California, 1973.
- ⁴Sachs, G., “Minimum Shear Wind Strength Required for Dynamic Soaring of Albatrosses,” *Ibis*, Vol. 147, 2005, pp. 1–10.
- ⁵Barnes, J. P., “How Flies the Albatross – the Flight Mechanics of Dynamic Soaring,” SAE Paper 2004–01–3088, November 2004.
- ⁶Lissaman, P., “Wind Energy Extraction by Birds and Flight Vehicles,” AIAA Paper 2005–241, January 2005.
- ⁷Denny, M., “Dynamic Soaring: Aerodynamics for Albatrosses,” *European Journal of Physics*, Vol. 30, 2009, pp. 75–84.
- ⁸Sachs, G. and da Costa, O., “Optimization of Dynamic Soaring at Ridges,” AIAA Paper 2003–5303, August 2003.
- ⁹Zhao, Y. J., “Optimal Patterns of Glider Dynamic Soaring,” *Optimal Control Applications and Methods*, Vol. 25, 2004, pp. 67–89.
- ¹⁰Akhtar, N., Whidborne, J. F., and Cooke, A. K., “Wind Shear Extraction Using Dynamic Soaring Techniques,” AIAA Paper 2009–7734, 2009.
- ¹¹Zhao, Y. J. and Qi, Y. C., “Minimum Fuel Powered Dynamic Soaring of Unmanned Aerial Vehicles Utilizing Wind Gradients,” *Optimal Control Applications and Methods*, Vol. 25, 2004, pp. 211–233.
- ¹²Gordon, R. J., *Optimal Dynamic Soaring for Full Size Sailplanes*, Master’s thesis, Department of Aeronautical and Astronautical Engineering, Air Force Institute of Technology, Wright-Patterson Air Force Base, Ohio, September 2006.
- ¹³Wurts, J., “Dynamic Soaring,” *Sailplane & Electric Modeler*, Vol. 3, No. 5, August–September 1998, pp. 52–53.
- ¹⁴Fogel, L., “Dynamic Soaring?” *Sailplane & Electric Modeler*, Vol. 4, No. 5, January 1999, pp. 94–97.
- ¹⁵Sachs, G. and Mayrhofer, M., “Dynamic Soaring Basics: Part 1, Model Gliders and Ridges,” *Sailplane & Electric Modeler*, Vol. 7, No. 10, December 2002, pp. 32, 36–37.
- ¹⁶Sachs, G. and Mayrhofer, M., “Dynamic Soaring Basics: Part 2, Minimum Wind Strength,” *Sailplane & Electric Modeler*, Vol. 8, No. 1, January 2003, pp. 82, 84–85.
- ¹⁷Boslough, M. B. E., “Autonomous Dynamic Soaring Platform for Distributed Mobile Sensor Arrays,” Sandia National Laboratories, SAND2002-1896, 2002.
- ¹⁸Parle, J., “Preliminary Dynamic Soaring Research Using a Radio Control Glider,” AIAA Paper 2004–132, January 2004.
- ¹⁹Sukumar, P. P., *Dynamic Soaring of Sailplanes in Open Fields*, Master’s thesis, Department of Aerospace Engineering, University of Illinois at Urbana-Champaign, Illinois, 2008.
- ²⁰Deittert, M., Richards, A., Toomer, C. A., and Pipe, A., “Dynamic Soaring Flight in Turbulence,” AIAA Paper 2009–6012, 2009.
- ²¹Stevens, B. L. and Lewis, F. L., *Aircraft Control and Simulation*, Wiley-Interscience, New York, NY, 2nd ed., 2003.
- ²²Stull, R. B., *An Introduction to Boundary Layer Meteorology*, Kluwer Academic Publishers, 1997.
- ²³“Department of Atmospheric Sciences, University of Illinois at Urbana-Champaign, Past 24 hours Champaign Weather,” last accessed 6/9/2010, <http://www.atmos.uiuc.edu/weather/daily/index.html>.
- ²⁴Marchaj, C. A., *Aero-Hydrodynamics of Sailing*, Dodd, Mead & Company, New York, NY, 1979.
- ²⁵Spera, D. A., *Wind Turbine Technology: Fundamental Concepts in Wind Turbine Engineering*, ASME, New York, NY, 2nd ed., 2009.
- ²⁶“FS One, Precision RC Flight Simulator,” Software, developed by InertiaSoft, distributed by Horizon Hobby, Champaign, IL, 2006.